



OPEN

Fast and selective reduction of nitroarenes under visible light with an earth-abundant plasmonic photocatalyst

Aby Cheruvathoor Poulouse¹✉, Giorgio Zoppellaro¹, Ioannis Konidakis², Efthymis Serpetzoglou², Emmanuel Stratakis², Ondřej Tomanec¹, Matthias Beller³, Aristides Bakandritsos^{1,4}✉ and Radek Zbořil^{1,4}✉

Reduction of nitroaromatics to the corresponding amines is a key process in the fine and bulk chemicals industry to produce polymers, pharmaceuticals, agrochemicals and dyes. However, their effective and selective reduction requires high temperatures and pressurized hydrogen and involves noble metal-based catalysts. Here we report on an earth-abundant, plasmonic nano-photocatalyst, with an excellent reaction rate towards the selective hydrogenation of nitroaromatics. With solar light as the only energy input, the chalcopyrite catalyst operates through the combined action of hot holes and photothermal effects. Ultrafast laser transient absorption and light-induced electron paramagnetic resonance spectroscopies have unveiled the energy matching of the hot holes in the valence band of the catalyst with the frontier orbitals of the hydrogen and electron donor, via a transient coordination intermediate. Consequently, the reusable and sustainable copper-iron-sulfide (CuFeS₂) catalyst delivers previously unattainable turnover frequencies, even in large-scale reactions, while the cost-normalized production rate stands an order of magnitude above the state of the art.

The effective transformation of organics into high added-value compounds is one of the pillars of a technologically advanced society^{1,2}. The reduction of nitroaromatics into amines, for example, is considered the key intermediate stage in the synthesis of dyes, polymers and many life-science products including anti-oxidants, pharmaceuticals and agrochemicals³. In general, aniline derivatives are synthesized industrially by the hydrogenation of nitroaromatics using noble metal-based thermal catalysts and H₂ pressurized gas as a reducing agent⁴, making such processes costly and potentially hazardous. Therefore, identifying sustainable catalysts with high activity for the reduction of nitroarenes under safer and eco-friendly conditions is a great challenge.

Advancements in reduction technologies of nitroarenes have demonstrated promising noble metal-free (photo)catalysts, such as transition metal oxides (Fe₂O₃ (ref. ⁵), Co₃O₄ (ref. ⁶), Cu₂O (ref. ⁷)), sulfides (Cu₂S (ref. ⁸) and CdS (ref. ⁹)), carbon-embedded metal species (Fe⁰/graphene-oxide¹⁰, Ni (ref. ¹¹), Co (refs. ^{12,13})) and coordination complexes (Fe-bipyridine¹⁴, Zn-based metal organic framework¹⁵). However, there are still limitations associated with low selectivity and reaction rates, with elevated reaction temperatures and irradiation intensities, need for pressurized H₂, long reaction times and limited recyclability^{5–7,9,11,16,17} (Supplementary Table 1).

Over the past decade, new insights into plasmon-enhanced nanocatalysis for organic transformations have attracted substantial attention offering improved selectivities, enhanced reaction rates and milder reaction conditions^{18,19}. Nevertheless, plasmonic catalysts are mostly based on costly noble metals, such as Au, Ag, Pd and Pt (refs. ^{18,20–23}). Furthermore, the desirable coordination of the reactants with the surface of such metallic nanoparticles is not favoured

due to the low surface reactivity of the latter, thus requiring the construction of multicomponent nanocatalysts^{19,24}. Ideally, a plasmonic photocatalyst should be endowed with intense plasmonic features but also with intrinsic catalytic activity through a strong interaction/coordination with the substrates. The second key limitation is related to the short-lived hot carriers and the difficulty of extracting this energy to perform a catalytic function, which currently attracts profound attention²⁵. Identifying pathways to effectively channel the energy from the plasmonic catalyst to the substrates is recognized as a critical aspect in achieving enhanced catalytic efficiencies^{25,26}. Recently, ternary chalcogenide nanocrystals (NCs) have stimulated research due to their low toxicity, earth abundance and tunable band gap²⁷. Among them, chalcopyrite (CuFeS₂) is a naturally occurring mineral having a bulk band gap of 0.5 eV and a tetragonal crystal structure, with tetrahedrally coordinated Cu¹⁺ and Fe³⁺ ions with sulfur^{28,29}. In the nano-form, CuFeS₂ NCs²⁹ exhibit localized surface plasmon resonance at 2.4 eV, resembling gold³⁰. CuFeS₂ NCs are nonemissive²⁸, and the excited surface plasmons dominantly relax through nonradiative damping because of the intermediate energy bands²⁹, generating hot electrons or holes and heat^{28,30}. Considering this and the high coordination proclivity of Fe-S units (ubiquitous in hydrogenases³¹) for hydrogen atoms and other organics, the CuFeS₂ NCs could represent an attractive plasmonic catalyst in reductive transformations—an aspect that has yet to be explored.

Here we report that CuFeS₂ NCs deliver excellent reaction rates towards the selective hydrogenation of nitroaromatics using hydrazine as a proton and electron donor, bypassing the need for noble metals, elevated temperatures, intense irradiation or H₂ gas. With solar light as the only energy input, the catalyst operates through the

¹Regional Centre of Advanced Technologies and Materials, Czech Advanced Technology and Research Institute, Palacký University, Olomouc, Czech Republic. ²Institute of Electronic Structure and Laser Foundation for Research and Technology-Hellas, Heraklion, Greece. ³Leibniz-Institute for Catalysis, Rostock, Germany. ⁴Nanotechnology Centre, Centre of Energy and Environmental Technologies, VŠB-Technical University of Ostrava, Ostrava-Poruba, Czech Republic. ✉e-mail: aby.cheruvathoorpoulouse@upol.cz; a.bakandritsos@upol.cz; radek.zboril@upol.cz

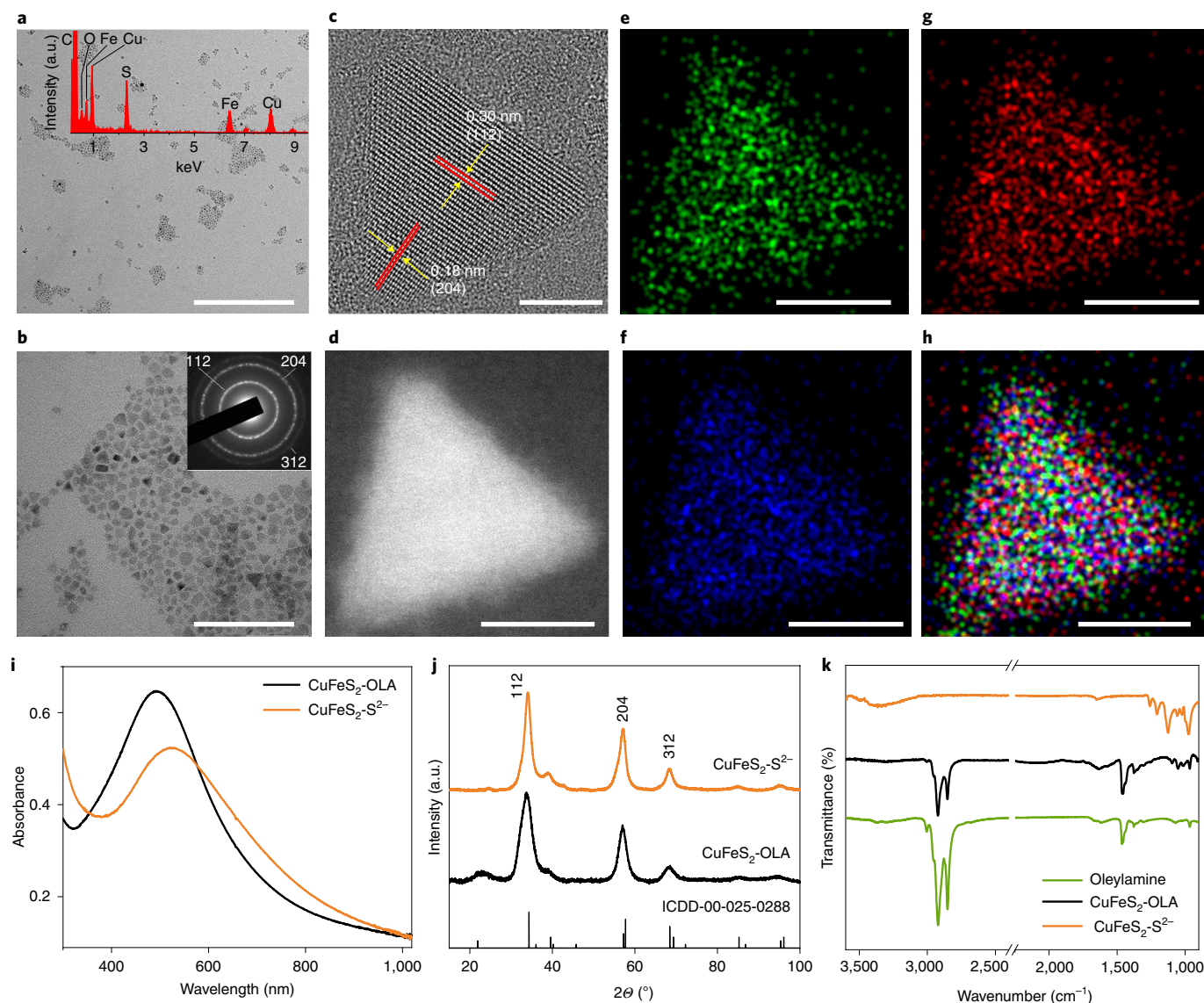


Fig. 1 | Structural identity of the CuFeS_2 NCs. **a,b**, TEM images of the CuFeS_2 NCs. Scale bars, 400 nm (**a**); 100 nm (**b**). Insets: the EDS (**a**); the selected area electron diffraction of the NCs (**b**). **c**, High-resolution TEM image of a single NC with marked lattice fringes. Scale bar, 5 nm. **d-f**, High-angle annular dark field-scanning TEM image (**d**) of a single NC with the corresponding EDS chemical mapping for Cu (**e**), S (**f**) and Fe (**g**). Scale bars, 8 nm. **h**, Combined mapping for Cu, Fe and S. Scale bar, 8 nm. **i-k**, UV-vis absorption spectra (beam path-length, 1 cm) (**i**), XRD analysis (**j**) and FTIR spectra (**k**) of CuFeS_2 NCs before ($\text{CuFeS}_2\text{-OLA}$) and after ($\text{CuFeS}_2\text{-S}^{2-}$) the ligand exchange reaction. OLA, oleylamine.

combined action of hot hole/electron formation and photothermal conversion. Ultrafast laser transient absorption and light-induced electron paramagnetic resonance spectroscopies unveiled the energy matching of the catalyst's electron holes with the highest occupied molecular orbital (HOMO) of hydrazine, activating it for the hydrogenation of the nitro-group into the respective amine. As a result, the plasmonic CuFeS_2 photocatalyst delivers an outstanding turnover frequency (TOF), while the cost-normalized production rate appears to stand an order of magnitude above the state of the art. The potency of the catalyst is further increased because it keeps its activity even against demanding substrates with sensitive side-groups, as well as after recycling under conditions of its maximum production rate or in large-scale reactions.

Results and discussion

Characterization of CuFeS_2 NCs. Oleylamine-capped CuFeS_2 NCs displayed an average size of 8–10 nm, as indicated by transmission

electron microscopy (TEM) (Fig. 1a–c and Supplementary Figs 2 and 3). Energy dispersive X-ray analysis (EDS) (Fig. 1a, inset and Supplementary Fig. 3c) and elemental mapping with high-angle annular dark field-scanning TEM (Fig. 1d–h) confirmed the homogeneous distribution of Cu, Fe and S elements throughout the crystal. The selected area electron diffraction (Fig. 1b, inset) and the X-ray diffraction (XRD) pattern (Fig. 1j) showed the characteristic diffraction rings and reflections, respectively, of the (112), (204) and (312) lattice planes of the tetragonal CuFeS_2 phase²⁸, confirming the purity of the product. Ultraviolet–visible light (UV–vis) absorption spectra of the NCs (Fig. 1i) demonstrated broad absorption at 520 nm, attributed to the plasmon resonance of the CuFeS_2 NCs²⁸.

The oleylamine-capping agents of the CuFeS_2 NCs were exchanged with S^{2-} ions to render them more dispersible in polar solvents and improve the interactions with the reactants. UV-vis absorption spectra before and after the ligand exchange (Fig. 1i) indicated that the plasmonic band was only slightly broadened

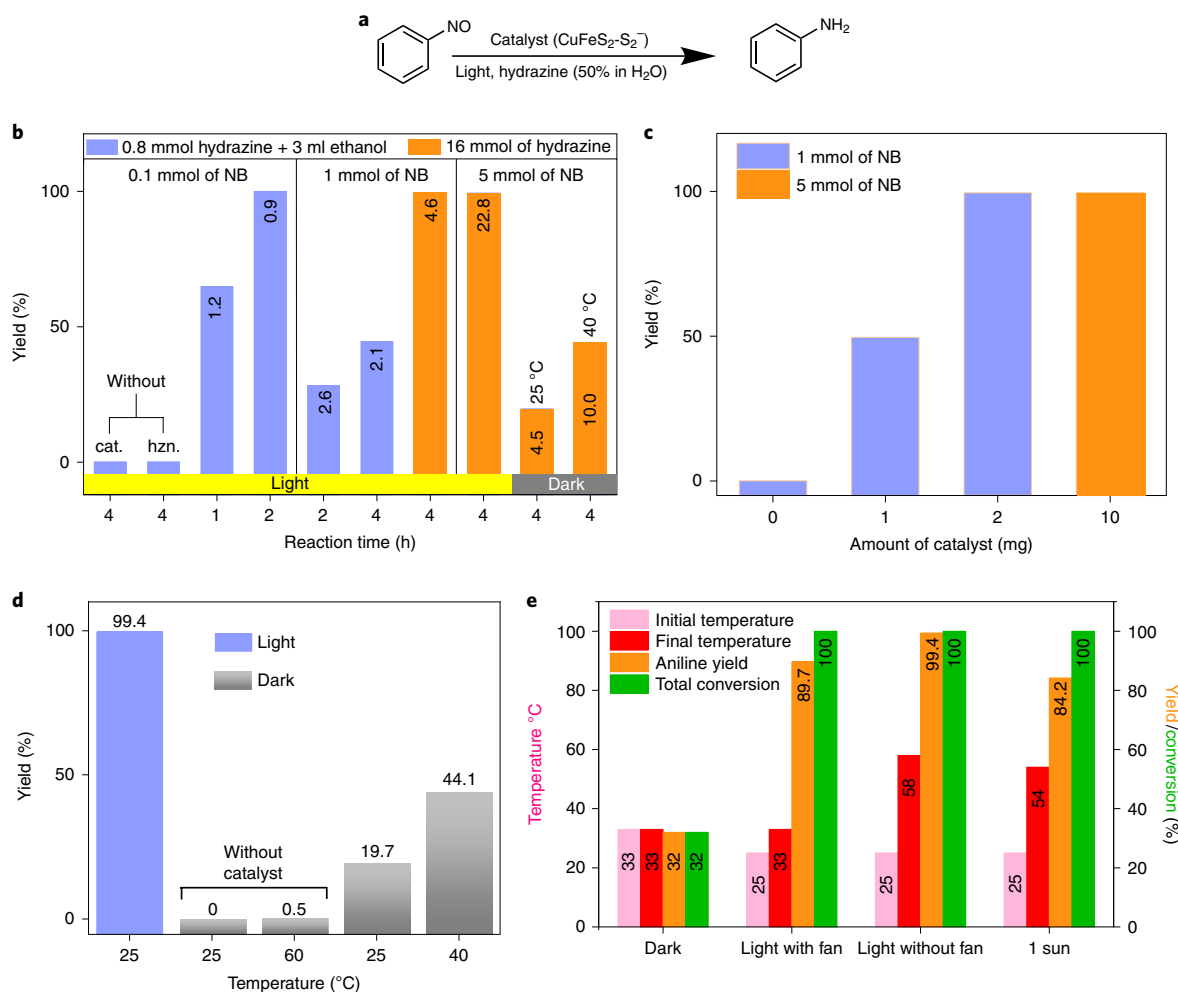


Fig. 2 | Catalytic reaction study. a–e, Reduction of nitrobenzene (NB) (a) using CuFeS_2 NCs (b) for different reaction times and amounts of NB and hydrazine hydrate, using in all cases 10 mg catalyst (labels inside the bars are the corresponding TOF values), with different catalyst amounts (c) (4 h reaction time), aniline yield at different environmental temperatures (d) (4 h, 16 mmol hydrazine, 5 mmol nitrobenzene, 10 mg catalyst) and under controlled temperature or light (e). Reaction conditions for e were nitrobenzene, 1 mmol; hydrazine hydrate, 1 ml; catalyst, 2 mg and under light/heat irradiation with continuous stirring for 4 h. cat., catalyst; hzn., hydrazine.

and red-shifted. XRD (Fig. 1j) and Raman spectra (Supplementary Fig. 4a) also confirmed the preservation of the crystal structure. The successful ligand exchange was confirmed with Fourier transform infrared spectroscopy (FTIR) (Fig. 1k), showing the elimination of the oleylamine spectral features at 2,987 and 2,900 cm^{-1} . Similarly, X-ray photoelectron spectroscopy (XPS) (Supplementary Fig. 4b) showed a dramatic reduction—or complete elimination—of the nitrogen peak (circled in red) in the $\text{CuFeS}_2\text{-S}^{2-}$ after removal of oleylamine. More details on the XPS characterization are available in Supplementary Fig. 5.

Photocatalytic performance of CuFeS_2 NCs. The photocatalytic activity of the CuFeS_2 NCs for the hydrogenation of nitroarenes (Fig. 2a) was evaluated using hydrazine hydrate as a hydrogen and electron donor. Hydrazine is an attractive choice because of the high hydrogen content (8.0 mass%), simply separable by-products (only hydrogen and nitrogen) and scalable synthesis from ammonia. The reaction was optimized under 400–500 nm of light, at a very low flux of 22 mW cm^{-2} and maximum intensity at 450 nm. Reaction optimization using 10 mg of the CuFeS_2 catalyst showed that at 2 h with 0.8 mmol of hydrazine afforded the product (aniline) at 100% yield and selectivity, using 0.1 mmol of the nitrobenzene substrate

(Fig. 2b, left part). By increasing the amount of the substrate tenfold (1 mmol) and the amount of hydrazine to 16 mmol (in 1 ml of H_2O) similar results were obtained at 4 h of reaction (Fig. 2b, middle part), corresponding to a molar TOF of 4.6 h^{-1} , this being already among the highest reported (Supplementary Table 1; TOF is calculated with respect to the total moles of all components of the catalyst, as explained in the notes of the same Table 1). It was very gratifying to observe that by further challenging the catalyst via increasing the substrate to 5 mmol under the exact same conditions, aniline was again obtained at 100% conversion and selectivity, affording the highest TOF value of 22.8 h^{-1} (Fig. 2b, right part). Reactions without catalyst or without hydrazine did not yield any aniline, while a control reaction in the dark at 25 °C delivered a yield of 19% (Fig. 2b), suggesting intrinsic catalytic activity of the system. CuFeS_2 NCs coated with the oleylamine molecules (Supplementary Fig. 7) showed lower yield than the S^{2-} passivated NCs. The reaction yield and rate depended on the amount of the catalyst (Fig. 2c) reaching a maximum yield of 99.4% and a molar average TOF of 22.8 h^{-1} with an optimum catalyst to substrate ratio of 10 mg per 5 mmol of nitrobenzene. This TOF is substantially higher than any recently disclosed state of the art thermal catalyst or photocatalyst for nitroarene reduction, as later discussed and described in Supplementary Table 1.

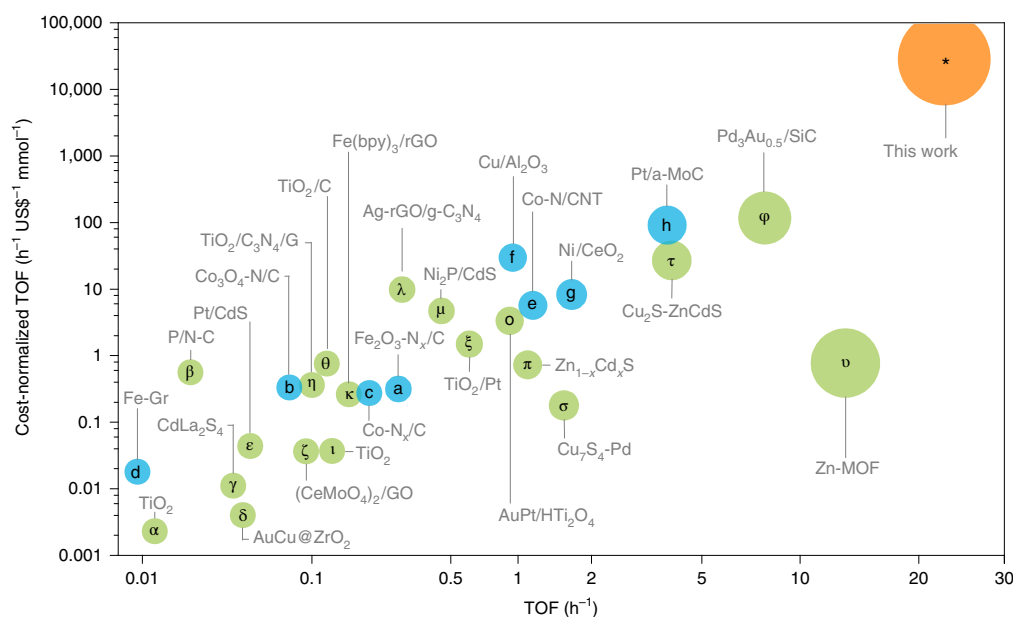


Fig. 4 | The catalyst performance with respect to the state of the art. Comparisons of the average TOF values and of the cost-normalized TOF for the CuFeS_2 catalyst and for previously reported ones, under photocatalytic conditions (Greek alphabet letters in green) and under elevated temperature and H_2 pressure conditions (Latin alphabet letters in blue). α , ref. ⁴⁰; β , ref. ⁴¹; γ , ref. ⁴²; δ , ref. ²³; ϵ , ref. ⁴³; ζ , ref. ⁴⁴; η , ref. ⁴⁵; θ , ref. ⁴⁶; ι , ref. ⁴⁷; κ , ref. ¹⁴; λ , ref. ⁴⁸; μ , ref. ¹⁶; ξ , ref. ⁴⁹; σ , ref. ²¹; π , ref. ⁹; σ , ref. ⁸; τ , ref. ¹⁷; ν , ref. ¹⁵; ϕ , ref. ²²; a , ref. ⁵; b , ref. ⁶; c , ref. ¹³; d , ref. ¹⁰; e , ref. ¹²; f , ref. ⁷; g , ref. ¹¹ and h , ref. ⁵⁰; more details are given in Supplementary Table 1.

4-iodo-nitrobenzoate and 4-ethynynitrobenzene^{5,6}) were obtained with yields of 99, 93.8 and 86.1%, respectively. Indicatively, previously achieved yields of 4-nitrobenzotrile and 4-ethynynitrobenzene were 75 (ref. ⁵) and 83% (ref. ⁶), respectively, at high temperature and 50 bar H_2 atmosphere.

Benchmarking of the catalyst. To interpret our results within the context of the current state of the art and with respect to the related costs, we collected data on the TOF values as well as on TOF with respect to the cost of the catalyst (Supplementary Table 1 and Fig. 4). For an unambiguous comparison, we included the whole catalyst system for calculating the TOF; regarding the price, we took into account the initial key reagents used in the synthesis of the catalysts, considering 100% yield (details are given in the Supplementary Table 1, in the Experimental section in the Supplementary Information). According to this analysis, the present CuFeS_2 - S^{2-} plasmonic photocatalyst revealed its high production rate and a transformative performance based on TOF with respect to the catalyst costs (Fig. 4).

Insights into the mechanism of action of the CuFeS_2 plasmonic photocatalyst. To better understand the high activity of the catalyst, ultrafast laser time-resolved transient absorption spectroscopy (TAS) and continuous-wave light-induced electron paramagnetic resonance experiments were performed (Fig. 5). In TAS studies, the difference in optical density (ΔOD) at various time delays and wavelengths (Fig. 5a,b) revealed the presence of two main processes: (1) a photo-induced absorption (PIA) and (2) a photobleaching feature in the vicinity of 590 and 750 nm, respectively. The PIA profile is attributed to transitions from temporary occupied states in the intermediate bands to the conduction band^{28,29}, while the simultaneously observed photobleaching feature is attributed to transitions from the depleted valence band to states within the intermediate band^{28,29}.

The decay dynamics of these two relaxation processes unveiled that both PIA and photobleaching exhibited an identical two-step decay profile, with a fast component of few ps, followed by a slower component of several tens of ps (Fig. 5b). The fast time

component is related to the nonradiative intraband electron–electron and electron–phonon scattering relaxation processes taking place in the intermediate band and in the conduction band, which results in carrier cooling on transferring the excess energy of the excited electrons to the crystal lattice, ultimately leading to NC heating^{20,29,30,33}. The slower time component is attributed to the heat transfer to the surrounding environment of the nanoparticles^{20,29,30,33}. The very similar fast decay profiles of PIA and photobleaching features indicate that hot electrons and heat are generated in both the conduction band and the intermediate band. Although these timescales are beyond the fs processes of Landau damping (when hot electron–hole pairs are generated³³) and therefore cannot be observed, nonradiative plasmonic nanostructures (such as CuFeS_2) favour hot electron generation and heating^{20,30,33}. According to the theoretically calculated band structure of CuFeS_2 (ref. ³⁴), the intermediate band–conduction band gap is about 2 eV (Fig. 5c), corroborating the PIA feature at the spectral window around 590 nm (2.1 eV). The valence band–intermediate band gap is 0.7–1 eV, matching the photobleaching feature with maximum around 910 nm, which was also verified by the Tauc plots, at around 0.85 eV (Supplementary Fig. 15). The full agreement between the experimental and theoretical data clearly supports the formation of holes in the valence band of CuFeS_2 (with maximum energy of around -5.2 eV³⁵) and hot electrons in the intermediate band and conduction band (at around -4 eV and above -2 eV, respectively, Fig. 5c). At the same time, the HOMO of hydrazine is positioned at -5.1 eV (ref. ³⁶), extremely close to the upper valence band energy levels of CuFeS_2 , where the holes are created. This energy matching promotes a favourable interaction of hydrazine’s antibonding and bonding HOMO electrons with the holes from CuFeS_2 valence band (generated during photoexcitation), which leads to weakening the N–H bond, proton and electron abstraction from hydrazine via formation of the intermediate complex, as depicted in the possible structure of Fig. 5d. Through continuous-wave light-induced electron paramagnetic resonance experiments, we observed such an interaction and electron transfer from hydrazine

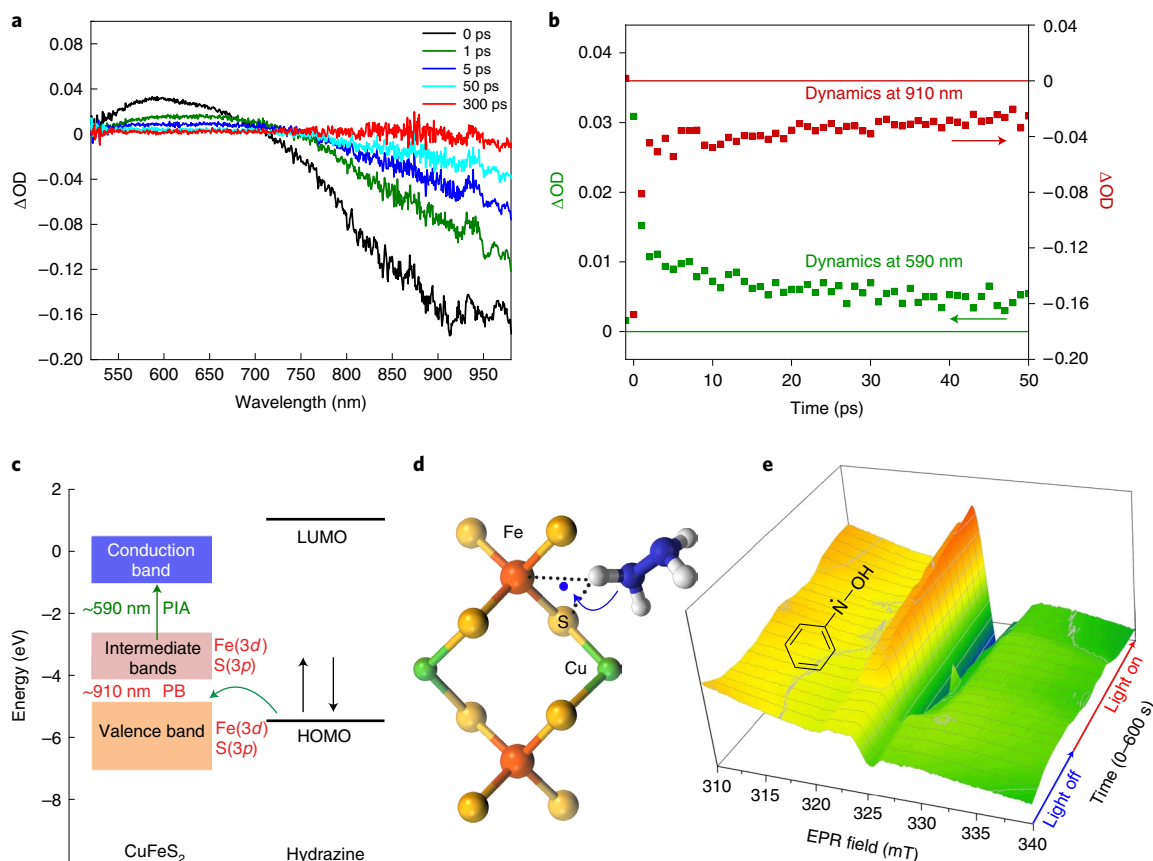


Fig. 5 | TAS and light-induced electron paramagnetic resonance studies of the catalyst. a, Time-resolved transient absorption spectra of the CuFeS_2 catalyst showing the optical density difference (ΔOD) as a function of wavelength at various time delays. **b**, Transient dynamics of the CuFeS_2 PIA at 590 nm and photobleaching (PB) at 910 nm. **c**, Schematic representation of energy level diagrams of CuFeS_2 and hydrazine. LUMO, lowest occupied molecular orbital. **d**, The photoexcited intermediate species of the catalyst with hydrazine, in accordance with hydrazine's oxidation by transferring electrons from its HOMO to the energy-matching photogenerated holes in the valence band of CuFeS_2 (**c**). **e**, The emergence of the three-electron reduction intermediate of nitrobenzene upon light irradiation.

to the catalyst in water before the addition of nitrobenzene, revealing a new photoexcited spin state (Supplementary Figs. 20 and 21) with hyperfine parameters suggesting the structure of Fig. 5d (and Supplementary Fig. 21e). On the addition of nitrobenzene, a new radical species produced a strong signal as time evolved (Fig. 5e and Supplementary Figs. 22 and 23). This type of signal corresponds to *N*-phenylhydroxylamine radical species ($-\text{N}^{\bullet}\text{-OH}$), as verified by the simulated spectrum with the corresponding spin-Hamiltonian parameters (Supplementary Fig. 23d) and by the spin-trap experiments (Supplementary Fig. 24). This radical can be associated with the three-electron reduced intermediate form of nitrobenzene (highlighted in the reaction mechanism in Supplementary Fig. 27), identifying a possible and previously elusive three-electron intermediate in the overall reaction pathway A. Further support for the predominance of pathway A in the presence of light is provided by gas chromatography results, showing hydroxylamine or azoxybenzene as the only stable intermediates in the presence of light or in the dark, respectively (Supplementary Fig. 28). The energy matching of the catalyst's photogenerated holes with the HOMO of hydrazine could be considered responsible for the excellent performance of the catalyst.

CuFeS_2 NCs also use the synergistic contribution of the two metal centres, Fe and Cu. The Fe site is responsible for binding and activating hydrazine, forming the transient spin-active species, $[\text{H}(\text{FeS}_2)\text{NH-NH}_2]^{\bullet}$, $S = 1/2$ system, which delivers the protons and electrons to the neighbouring $\text{Cu}(\text{I})\text{S}_2$ site. The $\text{Cu}(\text{I})\text{S}_2$ sites interact with the

nitro-substrate, producing the *N*-phenylhydroxylamine radical, as experimentally trapped in situ (Supplementary Fig. 23). The results take forward the concept that by a judicious combination of metal centres bound to rigid ligand-field environments, a highly effective catalytic system can be conveyed, harnessing the power of cooperative enzymatic catalytic centres³⁷, for example, to effectively transfer H^+ and e^- to the substrate³⁸. The use of the identified energy flow pair ($\text{CuFeS}_2\text{-H}_2\text{NNH}_2$) extends beyond this reaction, affecting a broad family of hydrogen transfer and reduction catalytic reactions in valuable processes for biomass valorization³⁹.

Conclusions

A highly efficient heterogeneous plasmonic photocatalyst is developed for the important catalytic reduction of nitroaromatics into amines, based on nontoxic and earth-abundant chalcopyrite NCs. The catalyst can spontaneously raise the reaction temperature and form photoexcited intermediate complexes with the reactants, delivering particularly high reaction rates even for demanding substrates with sensitive side-groups, as well as after its recycling under conditions of its maximum production rate. The production rate of this catalytic system is higher compared to other top-rated photo and thermal catalysts, with its cost-normalized rate standing an order of magnitude above the current state of the art. Surface modification of the catalyst with metal ions to tailor the energy of surface states and match the frontier orbitals of other substrates might further expand the importance and use of the present findings.

Online content

Any methods, additional references, Nature Research reporting summaries, source data, extended data, supplementary information, acknowledgements, peer review information; details of author contributions and competing interests; and statements of data and code availability are available at <https://doi.org/10.1038/s41565-022-01087-3>.

Received: 30 April 2021; Accepted: 7 February 2022;

Published online: 28 March 2022

References

- Ross, J. R. H. *Contemporary Catalysis: Fundamentals and Current Applications* (Elsevier, 2019).
- Romero, N. A. & Nicewicz, D. A. Organic photoredox catalysis. *Chem. Rev.* **116**, 10075–10166 (2016).
- Blaser, H. U. et al. Selective hydrogenation for fine chemicals: recent trends and new developments. *Adv. Synth. Catal.* **345**, 103–151 (2003).
- Corma, A. & Serna, P. Chemoselective hydrogenation of nitro compounds with supported gold catalysts. *Science* **313**, 332–334 (2006).
- Jagadeesh, R. V. et al. Nanoscale Fe₂O₃-based catalysts for selective hydrogenation of nitroarenes to anilines. *Science* **342**, 1073–1076 (2013).
- Westerhaus, F. A. et al. Heterogenized cobalt oxide catalysts for nitroarene reduction by pyrolysis of molecularly defined complexes. *Nat. Chem.* **5**, 537–543 (2013).
- Li, W. et al. General and chemoselective copper oxide catalysts for hydrogenation reactions. *ACS Catal.* **9**, 4302–4307 (2019).
- Cui, J. B. et al. Near-infrared plasmonic-enhanced solar energy harvest for highly efficient photocatalytic reactions. *Nano Lett.* **15**, 6295–6301 (2015).
- Kaur, M. & Nagaraja, C. M. Template-free synthesis of Zn_{1-x}Cd_xS nanocrystals with tunable band structure for efficient water splitting and reduction of nitroaromatics in water. *ACS Sustain. Chem. Eng.* **5**, 4293–4303 (2017).
- Goswami, A. et al. Fe(0)-embedded thermally reduced graphene oxide as efficient nanocatalyst for reduction of nitro compounds to amines. *Chem. Eng. J.* **382**, 122469 (2020).
- She, W. et al. High catalytic performance of a CeO₂-supported Ni catalyst for hydrogenation of nitroarenes, fabricated via coordination-assisted strategy. *ACS Appl. Mater. Interfaces* **10**, 17487–17487 (2018).
- Gong, W. B. et al. Nitrogen-doped carbon nanotube confined Co–N_x sites for selective hydrogenation of biomass-derived compounds. *Adv. Mater.* **31**, e1808341 (2019).
- Zhou, P. et al. High performance of a cobalt-nitrogen complex for the reduction and reductive coupling of nitro compounds into amines and their derivatives. *Sci. Adv.* **3**, e1601945 (2017).
- Kumar, A., Kumar, P., Paul, S. & Jain, S. L. Visible light assisted reduction of nitrobenzenes using Fe(bpy)₃²⁺/rGO nanocomposite as photocatalyst. *Appl. Surf. Sci.* **386**, 103–114 (2016).
- Chen, P. Q. et al. A visible-light-responsive metal-organic framework for highly efficient and selective photocatalytic oxidation of amines and reduction of nitroaromatics. *J. Mater. Chem. A* **7**, 27074–27080 (2019).
- Gao, W. Z., Xu, Y., Chena, Y. & Fu, W. F. Highly efficient and selective photocatalytic reduction of nitroarenes using the Ni₃P/CdS catalyst under visible-light irradiation. *Chem. Commun.* **51**, 13217–13220 (2015).
- Yu, Z. J. et al. Photocatalytic hydrogenation of nitroarenes using Cu_{1.94}S–Zn_{0.23}Cd_{0.77}S heteronanorods. *Nano Res.* **11**, 3730–3738 (2018).
- Gelle, A. et al. Applications of plasmon-enhanced nanocatalysis to organic transformations. *Chem. Rev.* **120**, 986–1041 (2020).
- Aslam, U., Rao, V. G., Chavez, S. & Linic, S. Catalytic conversion of solar to chemical energy on plasmonic metal nanostructures. *Nat. Catal.* **1**, 656–665 (2018).
- Furube, A. & Hashimoto, S. Insight into plasmonic hot-electron transfer and plasmon molecular drive: new dimensions in energy conversion and nanofabrication. *NPG Asia Mater.* **9**, e454 (2017).
- Song, Y. J. et al. Selective photocatalytic synthesis of haloanilines from halonitrobenzenes over multifunctional AuPt/monolayer titanate nanosheet. *ACS Catal.* **8**, 9656–9664 (2018).
- Hao, C. H. et al. Synergistic effect of segregated Pd and Au nanoparticles on semiconducting SiC for efficient photocatalytic hydrogenation of nitroarenes. *ACS Appl. Mater. Interfaces* **10**, 23029–23036 (2018).
- Xiao, Q. et al. Alloying gold with copper makes for a highly selective visible-light photocatalyst for the reduction of nitroaromatics to anilines. *ACS Catal.* **6**, 1744–1753 (2016).
- Aslam, U., Chavez, S. & Linic, S. Controlling energy flow in multimetallic nanostructures for plasmonic catalysis. *Nat. Nanotechnol.* **12**, 1000–1005 (2017).
- Linic, S., Chavez, S. & Elias, R. Flow and extraction of energy and charge carriers in hybrid plasmonic nanostructures. *Nat. Mater.* **20**, 916–924 (2021).
- Tagliabue, G. et al. Ultrafast hot-hole injection modifies hot-electron dynamics in Au/p-GaN heterostructures. *Nat. Mater.* **19**, 1312–1318 (2020).
- Regulacio, M. D. & Han, M. Y. Multinary I-III-VI₂ and I₂-II-IV-VI₄ semiconductor nanostructures for photocatalytic applications. *Acc. Chem. Res.* **49**, 511–519 (2016).
- Bhattacharyya, B. & Pandey, A. CuFeS₂ quantum dots and highly luminescent CuFeS₂ based core/shell structures: synthesis, tunability, and photophysics. *J. Am. Chem. Soc.* **138**, 10207–10213 (2016).
- Ghosh, S. et al. Colloidal CuFeS₂ nanocrystals: intermediate Fe *d*-band leads to high photothermal conversion efficiency. *Chem. Mater.* **28**, 4848–4858 (2016).
- Sugathan, A. et al. Why does CuFeS₂ resemble gold? *J. Phys. Chem. Lett.* **9**, 696–701 (2018).
- Britt, R. D., Rao, G. D. & Tao, L. Z. Bioassembly of complex iron-sulfur enzymes: hydrogenases and nitrogenases. *Nat. Rev. Chem.* **4**, 542–549 (2020).
- Zhang, X. et al. Product selectivity in plasmonic photocatalysis for carbon dioxide hydrogenation. *Nat. Commun.* **8**, 14542 (2017).
- Brongersma, M. L., Halas, N. J. & Nordlander, P. Plasmon-induced hot carrier science and technology. *Nat. Nanotechnol.* **10**, 25–34 (2015).
- Khaledialidusti, R., Mishra, A. K. & Barnoush, A. Temperature-dependent properties of magnetic CuFeS₂ from first-principles calculations: structure, mechanics, and thermodynamics. *AIP Adv.* **9**, 065021 (2019).
- Bastola, E., Bhandari, K. P., Subedi, I., Podraza, N. J. & Ellingson, R. J. Structural, optical, and hole transport properties of earth-abundant chalcopyrite (CuFeS₂) nanocrystals. *MRS Commun.* **8**, 970–978 (2018).
- Abdel-Latif, I. A. & Ammar, H. Y. Adsorption and magnetic properties of Cu₁MO₁₂ (M = Cu, Ni and Co): ab initio study. *Results Phys.* **7**, 4419–4426 (2017).
- Litman, Z. C., Wang, Y. J., Zhao, H. M. & Hartwig, J. F. Cooperative asymmetric reactions combining photocatalysis and enzymatic catalysis. *Nature* **560**, 355–359 (2018).
- Huang, G. F. et al. The atomic-resolution crystal structure of activated [Fe]-hydrogenase. *Nat. Catal.* **2**, 537–543 (2019).
- Yang, Y. J. et al. Porous organic frameworks featured by distinct confining fields for the selective hydrogenation of biomass-derived ketones. *Adv. Mater.* **32**, e1908243 (2020).
- Fukui, M., Koshida, W., Tanaka, A., Hashimoto, K. & Kominami, H. Photocatalytic hydrogenation of nitrobenzenes to anilines over noble metal-free TiO₂ utilizing methylamine as a hydrogen donor. *Appl. Catal. B* **268**, 118446 (2020).
- Zhang, H. et al. P/N co-doped carbon derived from cellulose: a metal-free photothermal catalyst for transfer hydrogenation of nitroarenes. *Appl. Surf. Sci.* **487**, 616–624 (2019).
- Zhang, S. et al. Photocatalytic organic transformations: simultaneous oxidation of aromatic alcohols and reduction of nitroarenes on CdLa₂S₄ in one reaction system. *Appl. Catal. B* **233**, 084 (2018).
- Zhang, S. J. et al. Ultra-low content of Pt modified CdS nanorods: preparation, characterization, and application for photocatalytic selective oxidation of aromatic alcohols and reduction of nitroarenes in one reaction system. *J. Hazard. Mater.* **360**, 182–192 (2018).
- Karthik, R. et al. A study of electrocatalytic and photocatalytic activity of cerium molybdate nanocubes decorated graphene oxide for the sensing and degradation of antibiotic drug chloramphenicol. *ACS Appl. Mater. Interfaces* **9**, 6547–6559 (2017).
- Zhang, L. Q. et al. Highly active TiO₂/g-C₃N₄/G photocatalyst with extended spectral response towards selective reduction of nitrobenzene. *Appl. Catal. B* **203**, 003 (2017).
- Xu, S. D., Tang, J. H., Zhou, Q. W., Du, J. & Li, H. X. Interfacing anatase with carbon layers for photocatalytic nitroarene hydrogenation. *ACS Sustain. Chem. Eng.* **7**, 16190–16199 (2019).
- Challagulla, S., Tarafder, K., Ganesan, R. & Roy, S. Structure sensitive photocatalytic reduction of nitroarenes over TiO₂. *Sci. Rep.* **7**, 8783 (2017).
- Kumar, A., Paul, B., Boukherroub, R. & Jain, S. L. Highly efficient conversion of the nitroarenes to amines at the interface of a ternary hybrid containing silver nanoparticles doped reduced graphene oxide/graphitic carbon nitride under visible light. *J. Hazard. Mater.* **387**, 121700 (2020).
- Kong, L., Mayorga-Martinez, C. C., Guan, J. G. & Pumera, M. Fuel-free light-powered TiO₂/Pt Janus micromotors for enhanced nitroaromatic explosives degradation. *ACS Appl. Mater. Interfaces* **10**, 22427–22434 (2018).
- Lin, L. L. et al. A highly CO-tolerant atomically dispersed Pt catalyst for chemoselective hydrogenation. *Nat. Nanotechnol.* **14**, 354–361 (2019).

Publisher's note Springer Nature remains neutral with regard to jurisdictional claims in published maps and institutional affiliations.



Open Access This article is licensed under a Creative Commons Attribution 4.0 International License, which permits use, sharing, adaptation, distribution and reproduction in any medium or format, as long as you give appropriate credit to the original author(s) and the source, provide a link to

the Creative Commons license, and indicate if changes were made. The images or other third party material in this article are included in the article's Creative Commons license, unless indicated otherwise in a credit line to the material. If material is not included in the article's Creative Commons license and your intended use is not permitted by

statutory regulation or exceeds the permitted use, you will need to obtain permission directly from the copyright holder. To view a copy of this license, visit <http://creativecommons.org/licenses/by/4.0/>.
© The Author(s) 2022

Methods

Supplementary Information files contain detailed descriptions of the methods used in this study.

Data availability

All data that support the findings of this study are available in the main text, figures and Supplementary Information files. Further data enquiries can be addressed to the corresponding authors on reasonable request. Source data are provided with this paper.

Acknowledgements

A.C.P. acknowledges the support from the European regional development fund (ERDF), European social fund (ESF) and The Ministry of Education, Youth and Sports of the Czech Republic, project no. CZ.02.2.69/0.0/0.0/20_079/0018294. The work was supported by the project Nano4Future (no. Z.02.1.01/0.0/0.0/16_019/0000754) financed from the ERDF and ESF. R.Z. acknowledges the funding from the Czech Science Foundation, project no. GA CR-EXPRO, 19-27454X. The Stratakis group acknowledges the funding from the European Union's Horizon 2020 Framework Programme for Research and Innovation under the NFFA-Europe-Pilot project (grant no. 101007417). We thank J. Stráská (TEM), M. Petr (XPS) and K. Štymplová (Raman) for the measurements.

Author contributions

A.C.P. was involved with the investigation, analysis, writing of the original draft, methodology and visualization. G.Z. was involved with the investigation, analysis, writing of the original draft, methodology and visualization. I.K. was involved with the investigation and analysis. E. Serpetzoglou was involved with the investigation. E. Stratakis was involved with the review and editing during writing. O.T. was involved with the investigation. M.B. was involved with the review and editing during writing. A.B. was involved with the supervision, writing of the original draft, visualization and review and editing during writing. R.Z. was involved with the supervision, funding acquisition and review and editing during writing.

Competing interests

The authors declare no competing interests.

Additional information

Supplementary information The online version contains supplementary material available at <https://doi.org/10.1038/s41565-022-01087-3>.

Correspondence and requests for materials should be addressed to Aby Cheruvathoor Poulouse, Aristides Bakandritsos or Radek Zbořil.

Peer review information *Nature Nanotechnology* thanks Rosa Llusar, Zehui Zhang and the other, anonymous, reviewer(s) for their contribution to the peer review of this work.

Reprints and permissions information is available at www.nature.com/reprints.